IGARSS 2023 - 2023 IEEE International Geoscience and Remote Sensing Symposium | 979-8-3503-2010-7/23/$31.00 ©2023 IEEE | DOI: 10.1109/IGARSS52108.2023.10282468

LINEAR MIXING MODEL PERFORMANCE WITH NONLINEAR EFFECTS IN HYPERSPECTRAL SUB-PIXEL TARGET DETECTION

Colin J. Maloney, John P. Kerekes, Emmett J. Ientilucci, and Chase Cañas

Rochester Institute of Technology
Chester F. Carlson Center for Imaging Science
54 Lomb Memorial Dr, Rochester, NY 14623

ABSTRACT

In the realm of hyperspectral sub-pixel target detection, the Linear Mixing Model (LMM) is an established basis for analysis and modelling. However, its accuracy depends on several key assumptions, most notably that there exists no nonlinear mixing within a scene. The Forecasting and Analysis of Spectroradiometric System Performance (FASSP) model utilizes the LMM to perform system requirement analyses. To quantify the limitations of the LMM when nonlinear effects are present, this paper reviews the results of September 2022 data collect in which the spectra of several sub-pixel target panels were altered by shadowing and reflectance panels and compares it with those from FASSP. Overall, both forms of nonlinear effects reduce target detection performance and the FASSP model tends to overestimate target radiance and target detection performance relative to the empirical results when nonlinear effects are present.

Index Terms— Hyperspectral imaging, remote sensing system modeling, linear mixing model, sub-pixel target detection, nonlinear mixing

1. INTRODUCTION

Since its conception with the first hyperspectral imagers in the early 1990s, remote Hyperspectral Imaging (HSI) has demonstrated a wide range of utilities from environmental spectroscopy to sub-pixel object detection in wavelengths stretching from the visible part (VIS) to the long wave infrared regions (LWIR) of the electromagnetic spectrum. Many techniques used for analyzing HSI data rely on the Linear Mixing Model (LMM), which proposes a linear interaction between incoming solar radiance and objects in a scene.

As it is so widely used as the underpinning of the modelling of the propagation of light to a sensor, characterizing the limitations of the LMM is a valuable undertaking. Our work focuses primarily on characterizing the impact of nonlinear effects from nearby brightly-colored panels and shadowing panels on the performance of the LMM. Of particular interest to this paper is exploring the shortcomings of the Forecasting and Analysis of Spectroradiometric System Performance (FASSP) model [1] with the presence of these nonlinear effects. To accomplish this, data from FASSP was compared to several experimental setups that were used during a September 2022 drone flight collect with a Nano-Hyperspec^{TM} sensor from Headwall Photonics [2] at the Tait Preserve, a private property owned by the Rochester Institute of Technology (RIT) in Rochester, New York.

Section 2 covers the basics of the LMM. Section 3 discusses the FASSP model and its input parameters. Section 4 explores the experimental design that was chosen in order to test the limitations of the LMM currently implemented in the FASSP model. Section 5 discusses the results of the collect and compares our findings to the predictions of FASSP. Finally, Section 6 summarizes our work and Section 7 presents the relevant future work currently being pursued.

2. LINEAR MIXING MODEL

The LMM is a widely used theoretical model that describes the interaction between light and materials within a scene on a macroscopic scale [3]. The LMM proposes that individual pixels within hyperspectral data which contain multiple materials can be represented as a linear combination of the spectra of those pure materials, $\rho(\lambda)$ weighted by the abundance of that material within that pixel, α [3]. The spectra of these pure materials are often called endmembers. In any real situation, additive noise from the sensor or nonlinear effects and are often represented by an additional term, n; which is a random vector with a mean, μ of zero. The LMM can also be represented in matrix form, where for m endmembers with k bands, $\mathbf{E}$ is a matrix containing the spectra of the included endmembers and with size of $k \times m$. $\mathbf{a}$ is a vector which represents the abundances of the endmembers within a pixel and with size $m \times 1$. Finally, $\mathbf{n}$ is a vector representing random noise and has size $k \times 1$. Eq. (1) shows the basic LMM model.

$$\mathbf{x_{pixel}} = \sum_{j=0}^{M} \alpha_j \rho_j(\lambda) + n = \mathbf{Ea} + \mathbf{n} \tag{1}$$

The LMM is based on at least two key assumptions: that

the response of a sensor is linear and that there exists no non-linear scattering within a scene. In our experiments, the first assumption was believed to be true, but the latter was violated in three out of four of our experimental setups with the placement of brightly colored treeshine reflector (TR) panels and shadowing (S) panels within the scene, which either contaminated the target spectra or shadowed the targets. More discussion of this will follow in Section 4. For target detection purposes, the LMM is applied to determine whether a given pixel has a large enough abundance of the target spectrum to be considered as a target pixel; the critical value is often determined by the Neyman-Pearson (NP) criterion, where the user sets an acceptable constant false alarm rate (CFAR) [3].

3. FASSP

The Forecasting and Analysis of Spectroradiometric System Performance (FASSP) model is a statistical-analytical model that simulates the detection of sub-pixel surface objects in a given background setup [1]. FASSP assumes that the various classes in a scene may be accurately represented by the first- and second- order spectral statistics and that an end-to-end HSI system may be modeled as the linear transform of those statistics.

Table 1: Relevant User Inputs for FASSP.

number of surface classes	$M \geq 2$
fraction of scene occupied by class m	$0 < f_m < 1$
fraction of pixel occupied by target class	$0 < f_{tgt} < 1$
fraction of target in shadow	$0 < f_{sh} < 1$
fraction of sky visible for shadowed target	$0 < f_{sky} < 1$
solar zenith angle	$0 \leq \theta_z < 90^\circ$
desired false alarm rate	P_{FA}

To make its predictions, FASSP assumes that the target class resides as a sub-pixel class within one of the background classes. FASSP operates with the assistance of MODerate resolution atmospheric TRANsmission (MODTRAN), which models the transmission of light through the atmosphere [4]. FASSP ultimately produces predicted target radiances and Receiver-Operating Characteristic (ROC) curves, which maps the expected probability of detection, $P(D)$, to a given probability of false alarm $P(FA)$ for a detector. FASSP takes user inputs to characterize a given scene to be simulated; the variables which are relevant to the scope of this work are shown in Table 1. In order to accurately simulate the experimental setups (to be described in Section 4), the fractions of the targets shadowed and the sky visible to the target, f_{sh} and f_{sky}, as well as the fractions of the scene occupied by the background and target classes, f_m and f_{tgt}, were varied from setup to setup accurately copy the empirical setups. For a full list of all of the user inputs available in FASSP and for more information on FASSP, see [1, 5].

FASSP can model the at-sensor spectral radiance, L_{ap}, for both reflected solar radiance and emitted radiance from the surface. For the purposes of this paper, only radiance in the VNIR/SWIR is relevant, which is shown in its simplest form by Eq. (2).

$$L_{ap} = \frac{\tau \rho_{DHR} E_s}{\pi} + \tau \rho L_d + L_a(\rho_{adj}) \tag{2}$$

τ is the atmospheric transmission, ρ_{DHR} is the directional hemispherical reflectance (DHR) of the material, E_s the direct solar irradiance, L_d is the diffuse downwelling solar radiance, and L_a is the path radiance. The path radiance is calculated with a reflectance variable that is a composite of all of the background DHR multiplied by their proportion of the scene, ρ_{adj}.

4. EXPERIMENTAL SETUP

On September 9, 2022, 11 drone flights with the Nano-Hyperspec™ were completed over Tait Preserve; four of those flights are pertinent to the focus of this paper. The weather on the day of the data collect was very clear and sunny; towards the latter end of the missions, however, some clouds began to arrive and so flights were completed only when the sun was not blocked.

The flights were all conducted from 10:31 to 13:30 Eastern Time (ET), during which time the solar zenith angle ranged from approximately 46° to 53°. The five targets used in each of these arrangements measured 3 ft $\times 4$ ft and possessed hexagonal cutouts of varying sizes in order to achieve predetermined sub-pixel fractions based on the Nano's Ground Sample Distance (GSD); which was about 4.5 centimeters [6]. The targets had fill fractions of approximately 100%, 80%, 60%, 40%, and 20% and were painted green. Figure 1 shows both the base and Treeshine Reflector - Shadowing panel (TR-S) setups. The other two setups are omitted from Figure 1 for the sake of brevity. Both the TR panel and the shadowing panel were constructed from a 4 ft $\times 4$ ft piece of Oriented Strand Board (OSB); the TR panel was painted bright red. These dimensions were chosen to ensure that the shadowing panels were large enough to shadow a majority of the green target with the predetermined solar zenith angle at the time of collection. A semi-matte paint was chosen to reduce the specular nature of the panel and to increase the probability of producing spectral contamination in the detected spectra of the green targets. The intent with the TR panels was to contaminate the spectra of the green targets, much like tree leaves and vegetation often contaminate the spectra of objects near them. To accomplish this,

Fig. 1: Two of the four target setups. The left image shows the base setup of green sub-pixel targets with no shadowing or TR panels. The 20% target is closest in the FOV. The right image shows the TR panel and shadowing panel (TR-S) setup. The other two arrangements were the shadowing panel setup - which consisted of the shadowing panel from the right image without the bright red TR panel, and the TR panel setup, which consisted of just the TR panel. The color contamination from the TR panel may be seen on the shadowing panel in the right image.

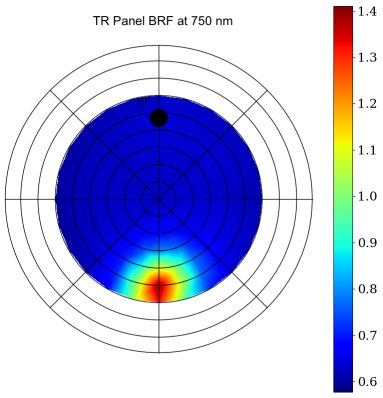

Fig. 2: The Bi-directional reflectance factor (BRF) of the Treeshine Reflector (TR) panel. Specular behavior is evidenced by the region of large reflectivity on the bottom of the diagram, where light is reflected in accordance with the law of reflection [3]. However, there also exists evidence of some diffuse behavior as shown by the yellowish regions of the diagram.

the panels needed to reflect the direct solar irradiance onto the green panels through both specular and diffuse means. It was also necessary to rotate the green target panels such that they were shadowed to the greatest extent possible. The right image in Figure 1 shows the slight rotation of the target panels in the TR-S setup. With a quick inspection of Figure 1 and 2 it should be apparent that despite all preparations, the panel still possessed a large specular reflective component. Figure 2 shows the Bi-directional reflectance factor (BRF) of the TR panel at 750 nanometers. These measurements were made using RIT's goniometer (GRIT-T) and were performed with a light source placed at $46.7°$ above the horizon, which was what the solar zenith angle was approximately 11:30 ET, when the TR-S setup was being imaged in our drone flights. GRIT-T uses an ASD FieldSpec4 High Resolution Spectrometer™ from Malvern Panalytical to measure the spectrum of a material over an entire hemisphere at constant intervals of various azimuth and zenith angles, which is used to construct the Bi-directional reflectance function (BRDF), or the BRF, which is a related quantity [7].

5. RESULTS

Data from the Tait Preserve drone flights went through several stages of pre-processing before the analysis was completed. The data was converted from digital counts (DC) to spectral radiance via the Nano's calibration procedure. The spectral radiance for the green target from FASSP was also extracted for comparison.

Figure 4 shows the spectral radiance of the 100% green target from the Tait data collect and FASSP for each of the four setups described in Section 4. FASSP was run with parameters that closely aligned with the data collect. Namely, the f_{sh} parameter was set to one for the shadowing and TR-S panel setups and the f_{sky} parameter was set to 0.75 for the shadowing and the TR panel setup and 0.50 for the TR-S panel setup. FASSP obtains a root-mean-square error (RMSE) of $0.23\frac{mW}{cm^2 sr \mu m}$ for the base setup, $0.55\frac{mW}{cm^2 sr \mu m}$ for the shadowing panel setup, $0.30\frac{mW}{cm^2 sr \mu m}$ for the TR panel setup, and $1.07\frac{mW}{cm^2 sr \mu m}$ for the TR-S panel setup. It is interesting to note that the empirical target radiance in the TR panel setup is brighter than the base setup; this probably resulted from the TR panel reflecting some additional solar irradiance onto the target panel, making it appear brighter over all wavelengths. In addition, FASSP estimates that the target panel is brighter than it actually is when shadowing is present - in the shadowing panel setup, FASSP overestimates spectral radiance at all wavelengths and in the TR-S panel setup, FASSP overestimates it up to about 700 nm and underestimates it at higher wavelengths, which could be indicative of the impact of the increased spectral radiance from the red TR panel at higher wavelengths in the empirical data.

ROC curves were also generated for each setup using the radiance data with a constrained energy minimization (CEM) algorithm [3], which computes scores for every pixel with $r_{CEM}(x) = \frac{(s-\mu)^T \mathbf{R^{-1}} (x-\mu)}{(s-\mu)^T \mathbf{R^{-1}} (s-\mu)}$ where s is the target spectrum, $\mathbf{R^{-1}}$ is the sample correlation matrix, μ is the background mean, and x is the pixel being analyzed. These are shown in Figure 3. Note that when there is no false alarms, $P(FA)$, in

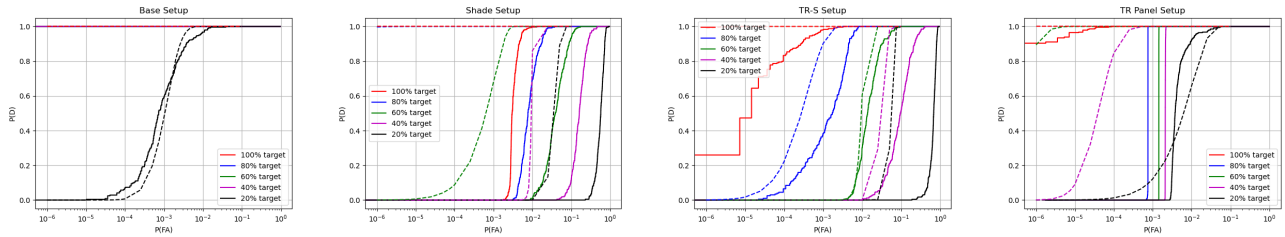

Fig. 3: ROC curve results from each of the setups from the drone data (solid lines) and from FASSP (dashed lines).

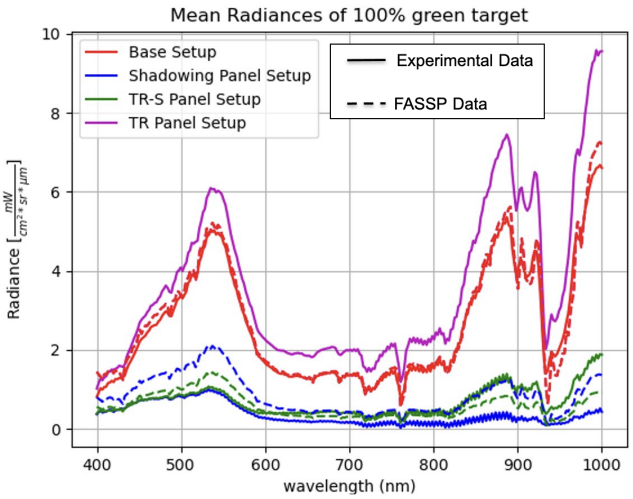

Fig. 4: The radiances of the 100% green target from the Tait data collect (solid lines) and FASSP (dashed lines). Note that FASSP predicts the same radiance values for the base and TR panel setups because there is no parameter input to describe the TR panel.

detecting the targets, the resulting ROC curve is just a horizontal line where $P(D) = 1$. It is apparent from these curves that target detection capability with the empirical data and with FASSP's predictions degrades when nonlinear effects are present. In addition, FASSP overestimates performance for the three setups where nonlinear effects are present.

6. CONCLUSIONS

Several experimental setups were designed and implemented to test the assumptions of the LMM by imposing controlled nonlinear effects on a basic subpixel target detection setup. The modelling performance of the LMM was assessed by comparing target spectral radiances and ROC curves from the data collect with a model based on the LMM, FASSP. The nonlinear effects were observed to negatively impact target dectection performance. In addition, when the nonlinear effects were present, FASSP overestimated target radiance and target detection performance.

7. FUTURE WORK

A 3-dimensional scene for Tait Preserve is currently in development within RIT's Digital Imaging and Remote Sensing Image Generation (DIRSIG), a 3-D path-tracing model [8], for comparison with the empirical observations. Work is also being conducted to determine methods to optimize FASSP to better consider nonlinear effects.

8. REFERENCES

[1] J.P. Kerekes and J.E. Baum, "Spectral Imaging System Analytical Model for Subpixel Object Detection," *IEEE TGRS*, vol. 40, no. 5, pp. 1088–1101, 2002.

[2] Headwall Photonics, "Headwall photonics," https://www.headwallphotonics.com, 2022.

[3] M. Eismann, *Hyperspectral Remote Sensing*, SPIE Press, Bellingham, Washington, 2012.

[4] A. Berk and et. al., "MODTRAN6: a major upgrade of the MODTRAN radiative transfer code," SPIE, 2014, vol. 9088, p. 90880H, SPIE.

[5] R. Zhao and Ientilucci, "A full-spectrum spectral imaging system analytical model with lwir tes capability," *IEE TGRS*, vol. 60, no. 5534409, pp. 1–9, 2022.

[6] Chase Cañas and et. al, "Empirical validation of a hyperspectral systems model for subpixel target detection using data from a new UAS field collection," vol. 12235, p. 122350E, SPIE.

[7] J. Harms, *The Design and Implementation of GRIT-T: RIT's Next-generation Field Portable Goniometer System*, Ph.D. thesis, Rochester Institute of Technology, 2016.

[8] A. Goodenough and S. Brown, "Dirsig5: Next-generation remote sensing data and image simulation framework," *IEEE JSTARS*, vol. 10, pp. 4818–4833, 11 2017.